ADVANCED OPTICAL MATERIALS
www.advopticalmat.de

Exciton Diffusion in Two-dimentional Chiral Perovskites

*Sophia Terres, Lucas Scalon, Julius Brunner, Dominik Horneber, Johannes Düreth, Shiyu Huang, Takashi Taniguchi, Kenji Watanabe, Ana Flávia Nogueira, Sven Höfling, Sebastian Klembt, Yana Vaynzof, and Alexey Chernikov**

Two-dimensional (2D) organic–inorganic hybrid perovskites emerged as a versatile platform for light-emitting and photovoltaic applications due to their unique structural design and chemical flexibility. Their properties depend heavily on the choice of the inorganic lead halide framework and the surrounding organic layers. Recently, the introduction of chiral cations into 2D perovskites has attracted major interest to induce chirality and tune the chiro-optical response. Importantly, their optical properties are dominated by tightly bound excitons that also serve as primary carriers for energy transport. The mobility of photo-injected excitons is thus important from the perspectives of fundamental material properties and optoelectronic applications, yet remains an open question. Here, exciton propagation in 2D chiral perovskites is demonstrated using transient photoluminescence microscopy and density-dependent transport over more than 100 nanometers at room temperature is revealed with diffusion coefficients as high as 2 $cm^2\ s^{-1}$. Two distinct regimes of initially rapid propagation and subsequent localization are observed. Moreover, perovskites with enantiomer pure cations exhibit faster exciton diffusion than the racemic mixture, correlated with the impact of the material composition on the disorder. Altogether, the observations of efficient exciton diffusion highlight the potential of 2D chiral perovskites to merge chiro-optical properties with strong light-matter interaction and energy transport.

1. Introduction

2D organic–inorganic hybrid perovskites, originally studied as early as the 1990s,[1–3] emerged as promising platforms for light-emitting[4–6] and photovoltaic applications.[7,8] These semiconducting materials feature an inorganic framework surrounded by organic layers with exceptional chemical and structural design flexibility.[9] The inorganic layers comprise corner-sharing lead halide octahedra and act as natural quantum wells hosting electronic states forming the conduction and valence bands.[10] The organic cations separate the inorganic layers and serve primarily as electronic barriers,[11,12] while also offering the possibility to integrate a variety of ammonium-based organic cations with different functional groups[13,14] and spatial configurations.[15–18] The ammonium groups bind to the halide of the inorganic framework via hydrogen bonds, while the organic moieties interact through van der Waals and π-stacking interactions.[19]

Recently, chiral organic cations were embedded into perovskites to generate

S. Terres, A. Chernikov
Institute of Applied Physics and Würzburg-Dresden Cluster of Excellence ct.qmat
TUD Dresden University of Technology
01062 Dresden, Germany
E-mail: alexey.chernikov@tu-dresden.de

L. Scalon, J. Brunner, Y. Vaynzof
Chair for Emerging Electronic Technologies
TUD Dresden University of Technology
01187 Dresden, Germany

L. Scalon, J. Brunner, Y. Vaynzof
Leibniz-Institute for Solid State and Materials Research Dresden
01069 Dresden, Germany

The ORCID identification number(s) for the author(s) of this article can be found under https://doi.org/10.1002/adom.202402606

DOI: 10.1002/adom.202402606

L. Scalon, A. F. Nogueira
Institute of Chemistry
University of Campinas (UNICAMP)
Campinas, São Paulo 13083-970, Brazil

D. Horneber, J. Düreth, S. Huang, S. Höfling, S. Klembt
Physikalisches Institut and Würzburg-Dresden Cluster of Excellence ct.qmat
Lehrstuhl für Technische Physik
Julius-Maximilians-Universität Würzburg
Am Hubland, 97074 Würzburg, Germany

T. Taniguchi
Research Center for Materials Nanoarchitectonics
National Institute for Material Science
1-1 Namiki, Tsukuba 305-0044, Japan

K. Watanabe
Research Center for Electronic and Optical Materials
National Institute for Materials Science
1-1 Namiki, Tsukuba 305-0044, Japan

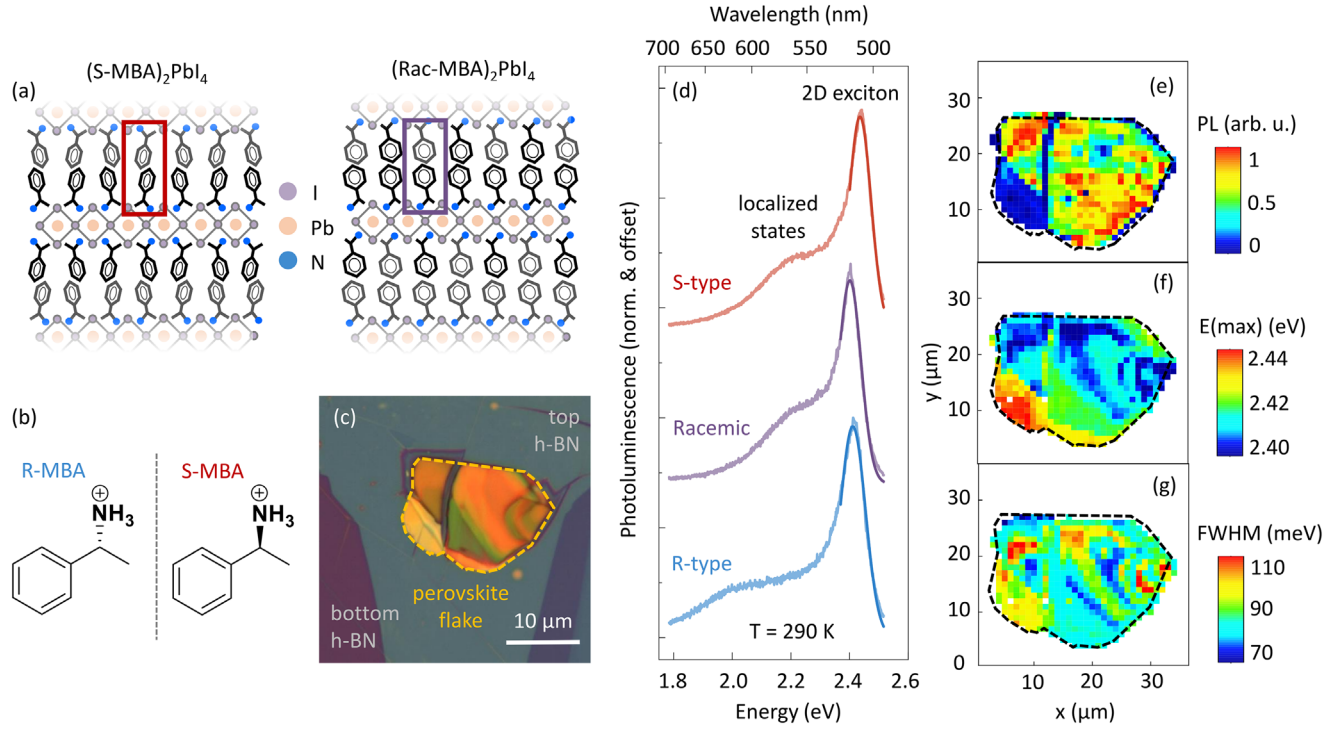

Figure 1. a) Schematic illustration of the layered structure of the (n = 1) chiral perovskite MBA_2PbI_4, consisting of alternating organic (methylbenzylammonium, MBA) and inorganic layers (PbI_4). Left panel: structure of the perovskite with enantiomer pure cations (S-MBA); right panel: perovskite structure with racemic mixture (Rac-MBA). b) Chemical structure of the enantiomers R-MBA and S-MBA. c) Optical micrograph of a typical thin-layer sample, encapsulated between 10's of nm thick layers of h-BN. d) Representative room temperature PL spectra of both S/R-type samples and the racemic mixture at a moderately high excitation fluence of 0.7 μJ cm^{-2} using 140 fs pulses with photon energy of 3.02 eV. Gaussian fits to the high energy flank of the peaks are indicated by solid lines on top of the data. Intrinsic 2D exciton PL and that attributed to localized states and 1D phase incursions are indicated. e) Maps of the room temperature PL intensity, f) PL peak energy and g) linewidth of the same R-type sample depicted in panel (c) with 1 μm step size, measured under continuous-wave 3.06 eV excitation.

chiro-optical responses,[20,21] which is highly interesting for polaritonics[22] and optospintronics.[23] Chiral cations were shown to induce structural chirality transfer across the interface between organic and inorganic units of 2D hybrid perovskites by breaking the centrosymmetry of the crystal.[24] This changes the electronic structure, introduces chiral polarization selection rules,[20] and impacts phase purity and electronic disorder.[25] Moreover, this class of materials inherits the combination of quantum confinement and reduced dielectric screening from the 2D perovskites, giving rise to strong Coulomb interactions between the charge carriers. Consequently, excitons with binding energies of several hundreds of meV form.[1,26,27] They represent fundamental electron-hole excitations with strong light-matter coupling,[28] dominate the optical response[29] and, most importantly, serve as primary energy carriers in these systems. Transport of optically injected excitons in chiral 2D perovskites is thus of major interest in the context of both fundamental physics of mobile and chiral many-body states and optoelectronic applications. In contrast to more conventional achiral 2D perovskites[30,31] however, the exciton propagation in chiral compounds, the underlying mechanisms of either free or localized transport, and their relationship to the material structure remain unexplored.

Here, we study exciton propagation in 2D chiral perovskites via transient photoluminescence microscopy. We observe linear and non-linear transport in samples with enantiomer pure (*R*- and *S*-configurations) cations and the racemic mixtures of both cations. The excitons are found to exhibit initially rapid diffusive transport over more than 100 nanometers at room temperature, followed by localization at later times. In addition, excitons propagate faster for all studied densities in perovskites with enantiomer pure cations than their racemic mixture counterpart. These findings correlate with different energy scales of disorder determined by photo-thermal deflection and hyperspatial spectroscopy.

2. Results

For this study, we used thin-layer samples exfoliated from chiral 2D methylbenzylammonium lead iodide crystals (MBA_2PbI_4). The crystals were synthesized under a nitrogen atmosphere by dissolving lead (II) oxide (PbO) in hydrogen iodide (HI), followed by dropwise addition of R-, S- or rac-methylbenzylamine.[25] Further details about the synthesis as well as X-ray diffraction patterns of these crystals are presented (Figure S1, Supporting Information) can be found in the Supporting Information. Structures of the enantiomer pure chiral 2D perovskite, as well as the racemic mixture, are schematically illustrated in **Figure 1a**. Enantiomer pure chiral cations induce the formation of asymmetric hydrogen bonds, creating symmetry-breaking distortions in the

inorganic framework.[15,24,32] Chemical structures of the cations producing crystallographic right- (R-MBA) and left-handedness (S-MBA) are displayed in Figure 1b. In the racemic mixture, consisting of equal parts S-MBA and R-MBA cations, the hydrogen bonds create symmetric tilting distortions, thus retaining the centrosymmetry of the crystal.[19,24]

The synthesized bulk crystals were micromechanically exfoliated, transferred onto SiO_2/Si substrates using a polymer stamp, and encapsulated between hexagonal boron nitride (h-BN) layers to ensure sample stability under illumination.[33] The resulting samples comprised of perovskite crystals of a few hundred nanometers thickness with tens of nanometers thick h-BN layers were placed in a microscopy cryostat for optical measurements under reduced pressure ($<10^{-4}$ bar). We used a continuous-wave laser with a photon energy of 3.06 eV for excitation in photoluminescence (PL) mapping and an 80 MHz, 140 fs pulsed Ti:sapphire laser with a photon energy of 3.02 eV for time- and spatially-resolved PL measurements. They were performed at room temperature, and the incident laser beams were focused onto the sample by a 60x microscope objective, resulting in spot sizes of about 0.5 µm. The PL signal was then dispersed using a grating or reflected by a mirror to obtain spectrally and spatially resolved responses. A CCD camera was used to record time-integrated signals and a streak camera was employed to monitor the time-resolved expansion of the emission area by imaging the luminescence cross-section along the x-coordinate. Additional details regarding sample preparation, cryogenic circularly polarized photoluminescence measurements and photo-thermal deflection spectroscopy are given in the Supporting Information.

2.1. Hyperspectral Mapping of Chiral 2D Perovskites

A micrograph of a studied thin-layer R-type sample encapsulated between two layers of h-BN is shown in Figure 1c. Typical room temperature PL spectra of all three sample types are presented in Figure 1d. They reveal the dominant 2D exciton signature at ≈2.4 eV with an asymmetric shoulder on the lower energy side, commonly associated with localized states[34] and 1D phase incursions.[35,36] While the use of the chiral cations enables the transfer of chirality, it also leads to steric hindrance for the interaction of the ammonium group with the inorganic core. This results in the formation of 1D moieties within the 2D perovskite, giving rise to broad-band emission at lower energies.[36,37]

The position of the main exciton peak and the lower energy shoulder are found to depend on the sample position and the underlying energy landscape, with variations up to a few tens of meV across the sample. We thus perform hyperspectral PL mapping to assess spatial variations of the exciton spectral features on the micrometer scale. Figure 1e–g displays maps of the PL intensity, peak energy and linewidth exemplary for an R-type sample (see SI for three additional R-type, S-type, and racemic mixture samples). Each pixel on the map corresponds to an individual PL spectrum. The values for the different parameters are extracted from Gaussian fits to the high energy flank of the 2D exciton resonance as indicated by solid lines in the respective colors in **Figure 2d**. The map of the extracted PL intensity reveals spot-to-spot variations on the order of 50%. They are partially related to fluctuations in material thickness across the exfoliated sample, as observed by the changes of color due to interference effects in the micrograph in Figure 1c. However, PL intensity also varies to a smaller degree in regions of seemingly uniform thickness, which is an observation not untypical for various 2D materials[38], including perovskites.[39] Analysis of the PL peak energy map shows an energy landscape featuring both homogeneous areas of comparatively flat potentials with deviations of only a few meV over many µm, but also variations between them. We observe local energy shifts of the exciton resonance on the order of 10 to 20 meV and overall shifts of up to 40 meV across the sample. Variations in the total linewidth within one measurement spot are on the same order of magnitude, reasonably agreeing with the inhomogeneities in the energy distribution on the larger scale. The differences in the room temperature linewidths in Figure 1d, dominated by scattering with phonons[40], are most likely caused by the disorder on the mesoscopic scale, prevalent in the studied chiral perovskites, as we show below. This represents the overall potential landscape for the excitons to propagate in the studied material.

2.2. Exciton Diffusion

To study exciton transport, we employ time- and spatially-resolved PL microscopy,[41,42] schematically illustrated in Figure 2a. Ultrafast laser pulses with excitation energy densities from 0.05 to 1.2 µJ cm^{-2} create a local distribution of excitons. The expansion of the light distribution emitted from the exciton cloud is then detected as a function of space and time. A typical PL transient of an S-type sample recorded at a moderate excitation density of 0.7 µJ cm^{-2} is presented in Figure 2b. It features a fast decay of the exciton population over the first several hundred ps after excitation and slower decay dynamics at later times. To analyze exciton transport across these regimes, we extract the broadening σ of the PL emission profiles from a Gaussian fit of the form $\exp[-x^2/2\sigma(t)^2]$. The resulting mean squared displacement $\Delta\sigma^2 = \sigma^2(t) - \sigma^2(0)$ is presented in Figure 2c as a function of time and exhibits two distinct propagation regimes.[43] At early times, we find a linear increase in the exciton spatial distribution, characteristic of diffusive transport.[41] At later times, the broadening of the PL emission reaches saturation, defining a second regime where the absence of spatial expansion indicates the localization of excitons as they get trapped in lower-energy sites.[34]

To analyze the subdiffusive behavior, we apply a model introduced by Seitz et al.[30] and Folie et al.[44], that considers initially free exciton propagation, followed by localization due to permanent capture of the excitons by deep traps. The model allows for extraction of the diffusion coefficient D from the mean squared displacement according to $\Delta\sigma^2(t) = 2\lambda_{eff}^2[1 - \exp(-\frac{D}{\lambda_{eff}^2}t)]$, where λ_{eff} is an effective average distance between traps.[30] The model was initially proposed to test the influence of trap states on the diffusion behavior in perovskites with achiral cations where the magnitude of the subdiffusive regime was found to be dependent on background illumination and excitation density.[30,43,45] For the studied chiral 2D perovskites, the obtained value for the diffusion coefficient of 1.2 cm^2 s^{-1} is very similar to findings in $(PEA)_2PbI_4$,[43,46] in which the organic cation is a constitutional isomer of MBA, known to exhibit comparatively

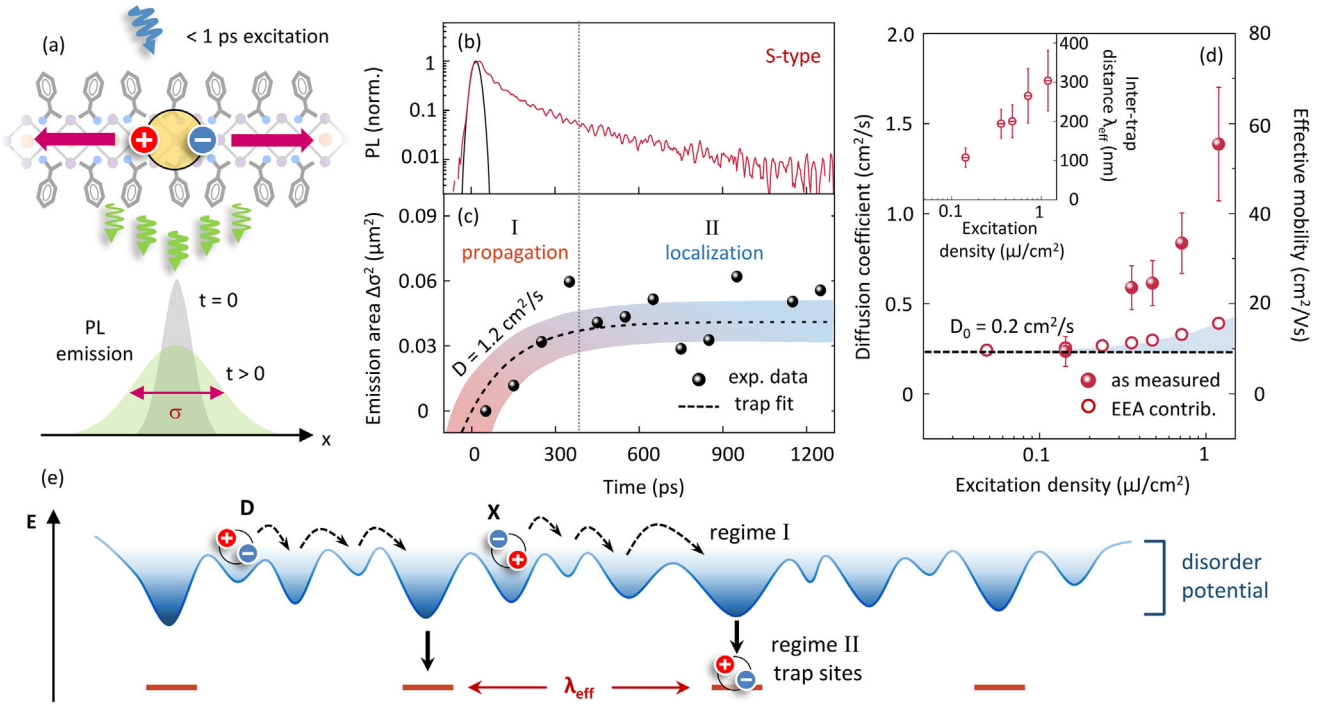

Figure 2. a) Schematic illustration of propagating excitons in the chiral perovskite MBA_2PbI_4 and the resulting emission, monitored via time- and spatially-resolved photoluminescence microscopy. b) Transient PL in an S-type sample, exhibiting initially rapid decay followed by slower dynamics. The black trace corresponds to the instrument response function of the streak camera for the chosen measurement mode. c) Corresponding mean-free displacement as a function of time, demonstrating a rapid increase during the first 100's ps characteristic for diffusive transport (regime I). It saturates at later times indicating localization (regime II). The dotted black vertical line serves as a separation between the two regimes (I & II). The diffusion coefficient D is extracted from the two-component propagation model according to Seitz et al.[30] and Folie et al.[44] of initial free propagation followed by localization into deep traps. Shaded area is a guide-to-the-eye. d) Diffusion coefficients as a function of excitation energy density demonstrating density-activated behavior. Estimated contribution of exciton-exciton annihilation (EEA) obtained from initial decay rate analysis shows negligible influence of this process. The black dashed line indicates the low-density diffusion coefficient D_0. The inset shows density-dependent increase of the effective inter-trap separation λ_{eff} extracted from the fit. e) Schematic illustration of excitons initially propagating freely through the disorder potential (regime I) with an effective diffusion coefficient D, followed by localization at deep trap sites (regime II) accounting for a decrease of the effective diffusivity at later times.

high diffusion in contrast to other 2D perovskites with different types of cations.[30,31] To test for non-linear processes at elevated fluences,[31] we performed diffusion measurements as a function of excitation energy density on the S-type sample. The results are shown in Figure 2d from low densities to the regime where the excitation starts to reduce relative PL intensity due to photo-bleaching. The diffusion coefficients increase linearly with excitation density, reaching up to 1.4 $cm^2\ s^{-1}$ (corresponding to an effective mobility of 55 cm^2/Vs calculating using the Einstein relation and classical approximation, presented for better comparison with electronic mobilities). This result starkly contrasts fluence-dependent measurements performed on $(PEA)_2PbI_4$, where diffusion coefficients remain nearly constant over more than three orders of magnitude in excitation density.[43,46] In general, density-activated diffusion can indicate the emergence of non-linear processes, such as exciton-exciton annihilation (EEA), leading to a strong increase in the observed diffusion coefficients and reduction of exciton lifetimes.[47,48]

We estimate the EEA coefficient by analyzing the initial decay rate of the PL after the excitation (see SI, Section 10) and determine the resulting effective diffusion coefficients according to $D_{eff} = D_0 + \frac{R_A \cdot n_0 \cdot w_0^2}{16}$. Here, R_A is the EEA coefficient, D_0 is the diffusion coefficient in the low-density limit and w_0 the width of the laser profile derived from the full-width-at-half maximum (FWHM) ($w_0 = \frac{FWHM}{2\sqrt{ln2}}$).[47] The determined R_A of $8 \times 10^{-3}\ cm^2\ s^{-1}$ would correspond to an increase of the effective diffusion coefficients of 0.15 $cm^2\ s^{-1}$ over the studied density range, accounting only for a negligible part of the observed increase. A similar analysis of excitation density dependence in R- and Rac-type samples yielded comparable results (see SI, Section 8). This means that exciton-exciton interactions only marginally contribute, and the non-linear diffusivity has a different origin in the studied samples.

Considering the presence of trapping sites that do not allow for detrapping, the aforementioned trap model permits the determination of an effective inter-trap distance for 100% capture probability.[30,49] The extracted values for the distance between trapping states are presented in the inset of Figure 2d as a function of excitation energy of the S-type sample. The effective inter-trap distance is in the range of a few 100's of nm. It increases linearly with the excitation density due to saturation, indicating that excitons are able to propagate further at

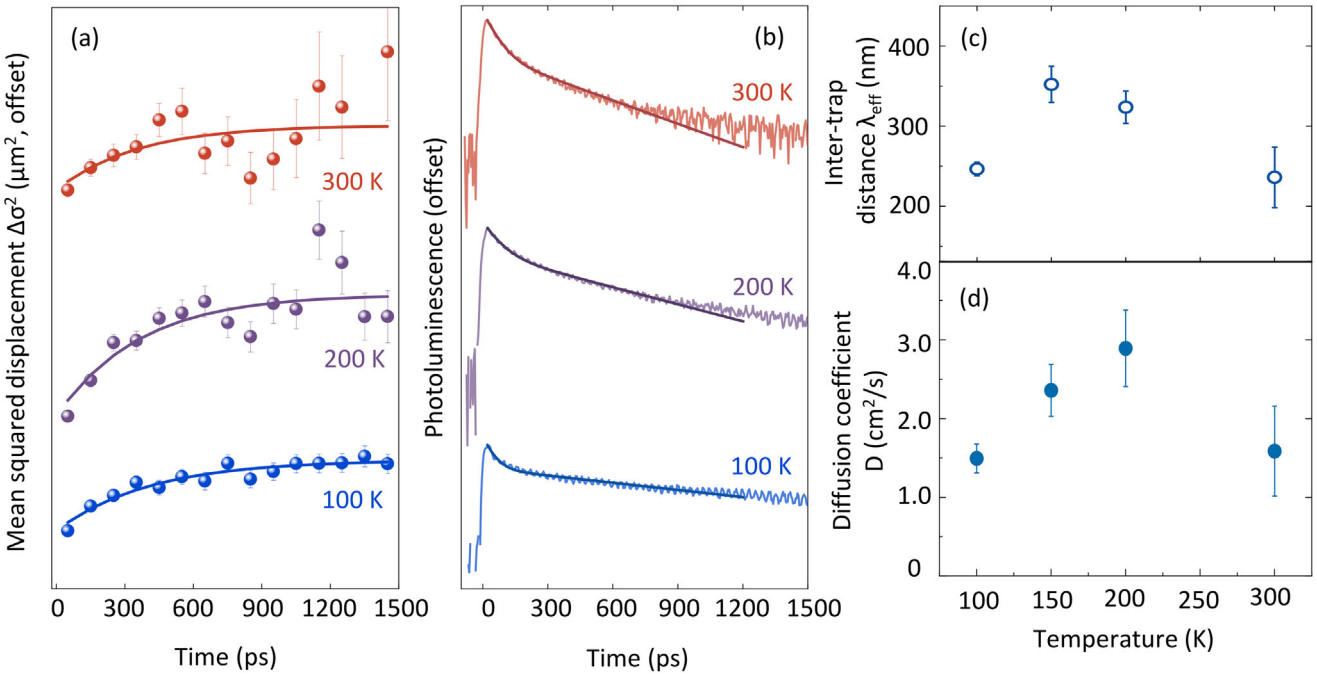

Figure 3. a) Mean squared displacement extracted from transient photoluminescence spectra of an S-type sample as a function of time, recorded at different temperatures and a fixed excitation density of 0.5 μJ cm^{-2} per pulse. Rapid broadening of the emission area over the first few 100 ps suggests initial efficient diffusive transport of excitons that is followed by localization at all studied temperatures. Solid lines represent fits from the two-component propagation model, accounting for initial free propagation and subsequent capture of excitons at trapping sites. b) Corresponding PL transients, demonstrating rapid recombination at early times, followed by decelerated decay dynamics in the localization regime. Solid lines represent biexponential fits to the data. c) Effective distance between trapping sites λ_{eff} as well as the d) diffusion coefficient D as a function of temperature. An increase of the effective inter-trap distance correlates with an increase of the diffusion coefficient, related to suppressed diffusion by earlier onset of the subdiffusive regime at lower temperatures.

elevated pump intensities before encountering active trapping sites. This finding implies that initial diffusion dynamics, in contrast to $(PEA)_2PbI_4$[30], are largely unaffected by deep trap density and are therefore more likely determined by the shallow disorder potential of the material. The observed increasingly faster exciton transport at higher excitation densities could then be attributed to gradual state filling within the disorder potential.[50] Figure 2e represent a schematic illustration of the proposed transport regimes: At early times after excitation, excitons are propagate freely with a diffusion coefficient D, determined by the disordered energy landscape and intrinsic scattering with the phonons. After several 100′s ps, excitons are captured by trapping sites that are sufficiently deep to not allow for detrapping and thus effectively decelerate the diffusivity in the second regime down to complete localization. At higher pump fluence, the deep traps are increasingly saturated, while the density-activated transport at early times is likely to stem from gradual filling of the states within the disordered energy potential with rising excitation density toward the excitonic mobility edge.

To better understand the exciton transport mechanisms, we perform temperature-dependent measurements at a fixed excitation density of 0.5 μJ cm^{-2} per pulse. **Figure 3a** depicts the mean squared displacements $\Delta\sigma^2$ obtained from time- and spatially resolved measurements of an S-type sample at 100, 200 and 300 K. Spatial broadening of the PL emission profiles over time shows similar behavior from 100 K up to room temperature, with a regime of initial increase over a few 100′s ps, followed by stagnation at later times. Both the initial expansion and the onset of the subdiffusive regime are only weakly temperature dependent and the applied model offers a reasonable description of the experimental data at all studied temperatures. The PL transients in Figure 3b as a function of temperature are consistent with the two distinct regimes. The first regime is characterized by fast exciton decay, while the second regime is determined by decelerated recombination kinetics. The extracted values for the effective inter-trap distance and the initial diffusion coefficient as a function of temperature are presented in Figure 3c,d, respectively. The diffusion coefficient slightly increases upon cooling down the sample from room temperature down to 200 K, characteristic for the free propagation regime. It decreases for temperatures below 200 K pointing at increased localization within the weakly disordered potential as the exciton transport starts to require thermal activation in this regime.[40,51] Nonetheless, the excitons remain reasonably mobile even at 100 K with the absolute diffusion coefficients being about two times smaller compared to the non-chiral 2D perovskites at similar conditions.[46] The corresponding changes in the inter-trap distance λ_{eff} is only weakly temperature-dependent with values between 250 and 350 nm for the chosen pump fluence. This seems reasonable, since the trap distance should be primarily related to the spacing between trapping sites and their saturation. It also means that the capture probability is only weakly dependent on the temperature in the studied range as well.

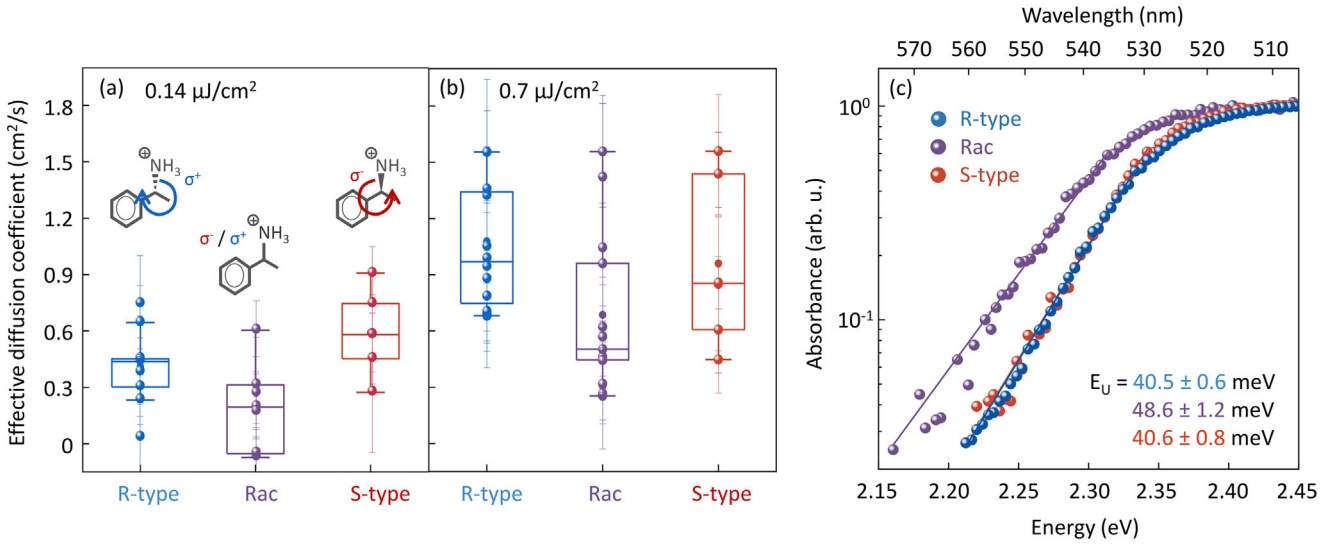

Figure 4. a) Summary of measured exciton diffusion coefficients recorded at low excitation density of 0.14 μJ cm^{-2} for all three sample types (R/Rac/S). The box plots display the interquartile range with the upper and lower quartiles representing the 25th and 75th percentiles, respectively. The line within each box indicates the median value, while the dot in the center represents the average. The box plots are superimposed with the diffusion coefficients of the corresponding individual measurements. b) Corresponding data for higher excitation fluence of 0.7 μJ cm^{-2}. c) Absorbance spectra from photothermal deflection measurements using thick crystals. The disorder is characterized by the Urbach energies E_U extracted from exponential fits (solid lines) and is correlated with the average diffusion coefficients.

2.3. Exciton Diffusion Across Different Chiralities

To investigate how structural changes to the inorganic framework affect exciton transport properties, we monitor propagation in enantiomer-pure perovskites (R/S-types) and the racemic mixture (Rac-type) at two distinct excitation fluences. The diffusion coefficient measurements recorded at low density (0.14 μJ cm^{-2}) are summarized in **Figure** 4a, and the ones measured at higher excitation energy fluence (0.7 μJ cm^{-2}) are shown in Figure 4b. The box plots display the interquartile range, with upper and lower quartiles being the 25th and 75th percentiles. The horizontal line in the center of the box indicates the median diffusion coefficient value for each sample type. The individual measurements are presented with the box plots and reach values up to 0.9 cm^2 s^{-1} even at low excitation densities while showing a considerable spread in all studied cases. We note that the observation of substantial fluctuations in the diffusion coefficient is not unusual in 2D hybrid perovskites.[46] It also aligns with the exciton peak's energy fluctuations determined by hyperspatial microscopy (see Figure 1f). Nevertheless, median transport coefficients show that the propagation of excitons in samples with enantiomer pure cations is faster than in racemic mixtures. This applies to low and high excitation fluence with S-type samples demonstrating the highest overall diffusion coefficients.

This observation points to structure-related differences in the exciton energy landscape, considering that chiral cations can introduce distortions to the inorganic framework. One of the metrics that is particularly sensitive to that is the detection of Urbach energies E_U used to quantify disorder in the crystal lattice. The parameter contains contributions from static and dynamic disorder and usually ranges from a few to several tens of meV in chiral 2D perovskites.[52] In amorphous semiconductors, the Urbach energy is mainly dominated by static disorder caused by variations in bond length and bond angle.[53] However, in perovskites such as $MAPbI_3$, a substantial contribution can also arise from the dynamic component due to the cage vibrations of the inorganic framework.[52,54]

To determine the disorder parameter E_U in the studied racemic mixtures compared to enantiomer pure crystals, we thus employ photo-thermal deflection spectroscopy using thick, large-area samples. The resulting absorbance spectra for all three sample types are presented in Figure 4c. The spectra exhibit an exponential decrease toward lower energies from excitonic tail states caused by defects in the crystal structure and lattice vibrations.[55] From exponential fits to the data, we extract Urbach energies of 40.5 and 40.6 meV for R- and S-type samples and 48.6 meV for the racemic mixture. Overall, the obtained values for the Urbach energies are somewhat larger compared to thin films of PEA_2PbI_4 with E_U = 35 meV[56] and MBA_2PbI_4 with E_U = 29 meV.[25] Most importantly, they naturally explain differences in the observed median diffusion coefficients between enantiomer pure 2D chiral perovskites and racemic mixtures.

3. Conclusion

In summary, we have experimentally demonstrated efficient exciton diffusion in single crystals of chiral 2D perovskites with values on the order of 1 cm^2 s^{-1} and the ability to efficiently transport energy over 100's of nm at room temperature. We identified two distinct regimes of initially rapid propagation within the first 0.5 ns and subsequent localization at later times. The studied crystals exhibited areas with homogeneous energy distribution on the order of several microns and tens of meV energy variations on larger spatial scales in accordance with the determined Urbach tail values. Moreover, excitons are found to propagate faster in perovskites with enantiomer pure cations compared to the

racemic mixture of both cations, which is linked to differences in disorder. Finally, we find a strong fluence dependence of the transport coefficients for all studied samples in contrast to other perovskites with similar, yet achiral cations, with only negligible impact of exciton-exciton annihilation. We attribute this behavior to the gradual filling of both deep traps and the states within the disorder potential with increasing excitation density, leading to increased fraction of freely propagating excitons. Observing comparatively fast room temperature exciton transport despite the presence of disorder renders chiral 2D perovskites an interesting platform for chiro-optical devices featuring mobile exciton quasiparticles. Alternatively, localization of excitons could be leveraged toward developing single-photon sources based on this class of chiral materials. Future developments toward increased excitonic mobility or the creation of exciton traps seem promising in view of the flexibility in the 2D perovskites' design.

4. Experimental Section

Synthesis: PbO (99.999%) purchased from Alfa Aesar Puratonic, hyroiodic acid (57 wt.%) from TCI chemicals and R-, S- and rac-methylbenzylamine as well as diethyl ether from Sigma–Aldrich were used. All chemicals were utilized without additional purification. The perovskites with R-, S- and rac-MBA cations were synthesized using the same procedure.[25] PbO (0.9 mmol) was dissolved in 5 ml of HI (57 wt.%) under N_2 atmosphere and magnetic stirring, followed by dropwise addition of R-/S-/rac-methylbenzylamine (1.8 mmol), leading to the formation of a precipitate. The reaction was then heated at 90 °C for 3 h to dissolve the precipitate. After that, stirring was stopped and the reaction mixture was cooled at a rate of 5 °C/30 min until it reached 30 °C. The orange, needle like crystals which formed overnight were vacuum filtered, washed with diethyl ether and underwent purification in a Soxhlet apparatus to remove HI residues. Finally, the crystals were dried in a vacuum oven for 4 h prior to use.

Exfoliation and Sample Fabrication: Single crystal 2D perovskite samples were fabricated via micro-mechanical exfoliation from bulk crystals and subsequent polymer-assisted stamping, following the technique outlined by Castellanos-Gomez et al.[57] Hexagonal boron nitride (h-BN) crystals were cleaved and thinned down using Scotch Magic Tape. Thinner crystals were transferred onto PDMS (polydimethylsiloxane) and then stamped onto preheated SiO_2/Si substrates. Perovskite flakes were produced in the same manner, transferred onto PDMS, aligned under a microscope and then stamped onto the previously deposited h-BN layer at room temperature to prevent temperature-induced degradation. The stack was completing by adding a second layer of h-BN, making sure that the perovskite was fully encapsulated from all sides for environmental protection.

Optical Spectroscopy: All measurements were performed with the samples mounted in a helium-flow cryostat (Cryovac) under high vacuum conditions to prevent oxygen-induced degradation of the samples. A continuous-wave solid state laser at a wavelength of 405 nm was used for time-integrated photoluminescence measurements. The laser was focused onto the sample using a glass-corrected 60x objective (Nikon), resulting in a spot size of ≈ 0.5 µm. The PL emission was filtered using hard-coated edge-pass filters (ThorLabs), dispersed by a grating spectrometer and detected by a Peltier-cooled charge-coupled device camera (Roper Scientific).

For spatially and time-resolved measurements, 140 fs pulses of an 80 MHz T-sapphire laser (Coherent) operating at 820 nm were frequency doubled by an SHG crystal (APE) and focused onto the sample via a glass-corrected 60x objective to a spot of ≈0.5 µm. The emitted signal passed through several spectral filters (ThorLabs) to eliminate reflected and scattered laser light. It was then focused onto the slit of an imaging spectrometer (Princeton Instruments), reflected by a silver mirror for spatially-resolved measurements and imaged onto a streak camera detector (Hamamatsu) providing temporal resolution. The streak camera was synchronized with the frequency of the Ti:sapphire laser and operated in single photon counting mode. For strong PL signals, neutral-density filters were employed to reduce intensity and prevent-double counting in the streak camera's single-photon detection.

Photothermal Deflection Spectroscopy: To assess large-area disorder, photo-thermal deflection spectroscopy (PDS) measurements were performed following established methods.[25,58] Millimeter-sized 2D perovskite flakes were mounted on UV-cured adhesive atop a quartz substrate and placed in a Fluorinert-filled cuvette. The sample was excited by a monochromator-filtered 150 W xenon short arc lamp (Ushio), while a 635 nm diode laser (ThorLabs) probed photothermal deflection. Absorbed light induced local heating, altering the refractive index and deflecting the laser beam, which was measured using a position-sensitive detector (ThorLabs) and lock-in amplifier (Amatec). The deflection directly correlated with film absorption, and Urbach energy was estimated by fitting the low-energy absorption tail.

Supporting Information

Supporting Information is available from the Wiley Online Library or from the author.

Acknowledgements

Financial support by the Deutsche Forschungsgemeinschaft (DFG) via SPP2196 Priority Program (Project-ID: 424709454), CRC1415 (Project-ID: 417590517, B11) and the Würzburg-Dresden Cluster of Excellence on Complexity and Topology in Quantum Matter ct.qmat (EXC 2147, Project-ID 390858490) is gratefully acknowledged. L.S. thanks the São Paulo Research Foundation (FAPESP), grants number 2020/04406-5 and 2021/12104-1. L.S. and A.F.N. acknowledge the support from FAPESP (grant Numbers 2017/11631-2 and 2018/21401-7), Shell, and the strategic importance of the support given by ANP (Brazil's National Oil, Natural Gas and Biofuels Agency) through the R&D levy regulation. Y.V. thank the DFG for funding in the framework of the Special Priority Program (SPP 2196) project PERFECT PVs (Project-ID: 424216076) and for generous support within the framework of the GRK 2767 (project A7). Part of the work was performed within the frame of the M-ERA.NET project PHANTASTIC (R.8003.22), supported by the SMWK. L.S. thanks the DFG for funding via the Walter Benjamin Program (Project-ID: 558721159). K.W. and T.T. acknowledge support from the JSPS KAKENHI (Grant Numbers 21H05233 and 23H02052) and World Premier International Research Center Initiative (WPI), MEXT, Japan. Deutsche Forschungsgemeinschaft (DFG): SPP2196 (424709454, 424216076); CRC1415 (417590517); GRK 2767; Excellence Cluster EXC 2147: 390858490; Sächsisches Staatsministerium für Wissenschaft, Kultur und Tourismus (SMWK): R.8003.22. The São Paulo Research Foundation (FAPESP): 2017/11631-2, 2018/21401-7, 2020/04406-5, 2021/12104-1; Japan Society for the Promotion of Science (JSPS): 21H05233, 23H02052; Brazil's National Oil, Natural Gas and Biofuels Agency (ANP); World Premier International Research Center Initiative (WPI).

Open access funding enabled and organized by Projekt DEAL.

Conflict of Interest

The authors declare no conflict of interest.

Author Contributions

A.C. and S.T. conceived the experimental idea, together with L.S. and Y.V. S.T. encapsulated the samples, and performed the hyperspectral mapping

and transient photoluminescence microscopy experiments. L.S, A.F.N., and Y.V. synthesized the perovskite crystals. K.W. and T.T. provided h-BN crystals. J.I.B. carried out the photothermal deflection spectroscopy measurements. D.H., J.D., Sh.Hu. Sv.Hö., and S.K. performed and analyzed circularly polarized photoluminescence measurements. The manuscript was written by S.T. and A.C. with input from all authors.

Data Availability Statement

The data that support the findings of this study are available from the corresponding author upon reasonable request.

Keywords

2D perovskites, chirality, diffusion, excitons, transient microscopy

Received: September 26, 2024
Revised: February 17, 2025
Published online: March 28, 2025

[1] T. Ishihara, J. Takahashi, T. Goto, *Solid State Commun.* **1989**, *69*, 933.
[2] D. B. Mitzi, C. A. Feild, W. T. A. Harrison, A. M. Guloy, *Nature* **1994**, *369*, 467.
[3] E. A. Muljarov, S. G. Tikhodeev, N. A. Gippius, T. Ishihara, *Phys. Rev. B* **1995**, *51*, 14370.
[4] S. Kumar, J. Jagielski, S. Yakunin, P. Rice, Y.-C. Chiu, M. Wang, G. Nedelcu, Y. Kim, S. Lin, E. J. G. Santos, M. V. Kovalenko, C.-J. Shih, *ACS Nano* **2016**, *10*, 9720.
[5] H. Tsai, W. Nie, J. Blancon, C. C. Stoumpos, C. M. M. Soe, J. Yoo, J. Crochet, S. Tretiak, J. Even, A. Sadhanala, G. Azzellino, R. Brenes, P. M. Ajayan, V. Bulović, S. D. Stranks, R. H. Friend, M. G. Kanatzidis, A. D. Mohite, *Adv. Mater.* **2018**, *30*, 1704217.
[6] N. Wang, L. Cheng, R. Ge, S. Zhang, Y. Miao, W. Zou, C. Yi, Y. Sun, Y. Cao, R. Yang, Y. Wei, Q. Guo, Y. Ke, M. Yu, Y. Jin, Y. Liu, Q. Ding, D. Di, L. Yang, G. Xing, H. Tian, C. Jin, F. Gao, R. H. Friend, J. Wang, W. Huang, *Nature Photon* **2016**, *10*, 699.
[7] G. Grancini, M. K. Nazeeruddin, *Nat. Rev. Mater.* **2018**, *4*, 4.
[8] H. Tsai, W. Nie, J.-C. Blancon, C. C. Stoumpos, R. Asadpour, B. Harutyunyan, A. J. Neukirch, R. Verduzco, J. J. Crochet, S. Tretiak, L. Pedesseau, J. Even, M. A. Alam, G. Gupta, J. Lou, P. M. Ajayan, M. J. Bedzyk, M. G. Kanatzidis, A. D. Mohite, *Nature* **2016**, *536*, 312.
[9] D. B. Mitzi, in *Progress in Inorganic Chemistry* (Ed.: K. D. Karlin), Wiley, Hoboken, New Jersey **1999**, pp. 1–121.
[10] L. M. Herz, *Annu. Rev. Phys. Chem.* **2016**, *67*, 65.
[11] T. Ishihara, J. Takahashi, T. Goto, *Phys. Rev. B* **1990**, *42*, 11099.
[12] C. M. Mauck, W. A. Tisdale, *Trends in Chemistry* **2019**, *1*, 380.
[13] F. Zhang, D. H. Kim, H. Lu, J.-S. Park, B. W. Larson, J. Hu, L. Gao, C. Xiao, O. G. Reid, X. Chen, Q. Zhao, P. F. Ndione, J. J. Berry, W. You, A. Walsh, M. C. Beard, K. Zhu, *J. Am. Chem. Soc.* **2019**, *141*, 5972.
[14] X. Zhao, M. L. Ball, A. Kakekhani, T. Liu, A. M. Rappe, Y.-L. Loo, *Nat. Commun.* **2022**, *13*, 3970.
[15] J. Ahn, E. Lee, J. Tan, W. Yang, B. Kim, J. Moon, *Mater. Horiz.* **2017**, *4*, 851.
[16] C. Han, A. J. Bradford, J. A. McNulty, W. Zhang, P. S. Halasyamani, A. M. Z. Slawin, F. D. Morrison, S. L. Lee, P. Lightfoot, *Chem. Mater.* **2022**, *34*, 2458.
[17] J. Lin, D. Chen, L. Yang, T. Lin, Y. Liu, Y. Chao, P. Chou, C. Chiu, *Angew Chem Int Ed* **2021**, *60*, 21434.
[18] J. Ahn, S. Ma, J.-Y. Kim, J. Kyhm, W. Yang, J. A. Lim, N. A. Kotov, J. Moon, *J. Am. Chem. Soc.* **2020**, *142*, 4206.
[19] L. Scalon, Y. Vaynzof, A. F. Nogueira, C. C. Oliveira, *Cell Reports Physical Science* **2023**, *4*, 101358.
[20] G. Long, C. Jiang, R. Sabatini, Z. Yang, M. Wei, L. N. Quan, Q. Liang, A. Rasmita, M. Askerka, G. Walters, X. Gong, J. Xing, X. Wen, R. Quintero-Bermudez, H. Yuan, G. Xing, X. R. Wang, D. Song, O. Voznyy, M. Zhang, S. Hoogland, W. Gao, Q. Xiong, E. H. Sargent, *Nature Photon* **2018**, *12*, 528.
[21] A. Pietropaolo, A. Mattoni, G. Pica, M. Fortino, G. Schifino, G. Grancini, *Chem* **2022**, *8*, 1231.
[22] Z. Wang, C. Lin, K. Murata, A. S. A. Kamal, B. Lin, M. Chen, S. Tang, Y. Ho, C. Chen, C. Chen, H. Daiguji, K. Ishii, J. Delaunay, *Adv. Mater.* **2023**, *35*, 2303203.
[23] J. Ma, H. Wang, D. Li, *Adv. Mater.* **2021**, *33*, 2008785.
[24] M. K. Jana, R. Song, H. Liu, D. R. Khanal, S. M. Janke, R. Zhao, C. Liu, Z. Valy Vardeny, V. Blum, D. B. Mitzi, *Nat. Commun.* **2020**, *11*, 4699.
[25] L. Scalon, J. Brunner, M. G. D. Guaita, R. Szostak, M. Albaladejo-Siguan, T. Kodalle, L. A. Guerrero-León, C. M. Sutter-Fella, C. C. Oliveira, Y. Vaynzof, A. F. Nogueira, *Adv. Opt. Mater.* **2024**, *12*, 2300776.
[26] K. Tanaka, T. Takahashi, T. Kondo, K. Umeda, K. Ema, T. Umebayashi, K. Asai, K. Uchida, N. Miura, *Jpn. J. Appl. Phys.* **2005**, *44*, 5923.
[27] O. Yaffe, A. Chernikov, Z. M. Norman, Y. Zhong, A. Velauthapillai, A. Van Der Zande, J. S. Owen, T. F. Heinz, *Phys. Rev. B* **2015**, *92*, 045414.
[28] D. B. Mitzi, K. Chondroudis, C. R. Kagan, *IBM J. Res. & Dev.* **2001**, *45*, 29.
[29] H. Haug, S. W. Koch, *Quantum Theory of the Optical and Electronic Properties of Semiconductors*, WORLD SCIENTIFIC, Singapore **2009**.
[30] M. Seitz, A. J. Magdaleno, N. Alcázar-Cano, M. Meléndez, T. J. Lubbers, S. W. Walraven, S. Pakdel, E. Prada, R. Delgado-Buscalioni, F. Prins, *Nat. Commun.* **2020**, *11*, 2035.
[31] S. Deng, E. Shi, L. Yuan, L. Jin, L. Dou, L. Huang, *Nat. Commun.* **2020**, *11*, 664.
[32] D. G. Billing, A. Lemmerer, *CrystEngComm* **2006**, *8*, 686.
[33] M. Seitz, P. Gant, A. Castellanos-Gomez, F. Prins, *Nanomaterials* **2019**, *9*, 1120.
[34] X. Wu, M. T. Trinh, D. Niesner, H. Zhu, Z. Norman, J. S. Owen, O. Yaffe, B. J. Kudisch, X.-Y. Zhu, *J. Am. Chem. Soc.* **2015**, *137*, 2089.
[35] J. Ma, C. Fang, C. Chen, L. Jin, J. Wang, S. Wang, J. Tang, D. Li, *ACS Nano* **2019**, *13*, 3659.
[36] L. Scalon, A. New, Z. Ge, N. Mondal, R. D. Campos, C. Quarti, D. Beljonne, A. F. Nogueira, A. A. Bakulin, Y. Vaynzof, *Chem. Mater.* **2024**, *36*, 4331.
[37] X. Li, J. M. Hoffman, M. G. Kanatzidis, *Chem. Rev.* **2021**, *121*, 2230.
[38] A. Neumann, J. Lindlau, L. Colombier, M. Nutz, S. Najmaei, J. Lou, A. D. Mohite, H. Yamaguchi, A. Högele, *Nature Nanotech* **2017**, *12*, 329.
[39] L. Niu, X. Liu, C. Cong, C. Wu, D. Wu, T. R. Chang, H. Wang, Q. Zeng, J. Zhou, X. Wang, W. Fu, P. Yu, Q. Fu, S. Najmaei, Z. Zhang, B. I. Yakobson, B. K. Tay, W. Zhou, H. T. Jeng, H. Lin, T. C. Sum, C. Jin, H. He, T. Yu, Z. Liu, *Adv. Mater.* **2015**, *27*, 7800.
[40] A. D. Wright, C. Verdi, R. L. Milot, G. E. Eperon, M. A. Pérez-Osorio, H. J. Snaith, F. Giustino, M. B. Johnston, L. M. Herz, *Nat. Commun.* **2016**, *7*, 11755.
[41] N. S. Ginsberg, W. A. Tisdale, *Annu. Rev. Phys. Chem.* **2020**, *71*, 1.
[42] G. M. Akselrod, P. B. Deotare, N. J. Thompson, J. Lee, W. A. Tisdale, M. A. Baldo, V. M. Menon, V. Bulović, *Nat. Commun.* **2014**, *5*, 3646.
[43] X. Xiao, M. Wu, Z. Ni, S. Xu, S. Chen, J. Hu, P. N. Rudd, W. You, J. Huang, *Adv. Mater.* **2020**, *32*, 2004080.
[44] B. D. Folie, J. A. Tan, J. Huang, P. C. Sercel, M. Delor, M. Lai, J. L. Lyons, N. Bernstein, A. L. Efros, P. Yang, N. S. Ginsberg, *J. Phys. Chem. A* **2020**, *124*, 1867.
[45] M. Maiberg, T. Hölscher, S. Zahedi-Azad, R. Scheer, *J. Appl. Phys.* **2015**, *118*, 105701.

[46] J. D. Ziegler, J. Zipfel, B. Meisinger, M. Menahem, X. Zhu, T. Taniguchi, K. Watanabe, O. Yaffe, D. A. Egger, A. Chernikov, *Nano Lett.* **2020**, *20*, 6674.
[47] M. Kulig, J. Zipfel, P. Nagler, S. Blanter, C. Schüller, T. Korn, N. Paradiso, M. M. Glazov, A. Chernikov, *Phys. Rev. Lett.* **2018**, *120*, 207401.
[48] S. Mouri, Y. Miyauchi, M. Toh, W. Zhao, G. Eda, K. Matsuda, *Phys. Rev. B* **2014**, *90*, 155449.
[49] M. Seitz, M. Meléndez, N. Alcázar-Cano, D. N. Congreve, R. Delgado-Buscalioni, F. Prins, *Adv. Opt. Mater.* **2021**, *9*, 2001875.
[50] H. Jin, E. Debroye, M. Keshavarz, I. G. Scheblykin, M. B. J. Roeffaers, J. Hofkens, J. A. Steele, *Mater. Horiz* **2020**, *7*, 397.
[51] B. I. Shklovskii, A. L. Ėfros, *Electronic Properties of Doped Semiconductors*, Springer-Verlag Berlin Heidelberg GmbH, Berlin Heidelberg **2013**.
[52] E. Ugur, M. Ledinský, T. G. Allen, J. Holovský, A. Vlk, S. De Wolf, *J. Phys. Chem. Lett.* **2022**, *13*, 7702.
[53] Y. Pan, F. Inam, M. Zhang, D. A. Drabold, *Phys. Rev. Lett.* **2008**, *100*, 206403.
[54] M. Ledinsky, T. Schönfeldová, J. Holovský, E. Aydin, Z. Hájková, L. Landová, N. Neyková, A. Fejfar, S. De Wolf, *J. Phys. Chem. Lett.* **2019**, *10*, 1368.
[55] V. M. Caselli, Z. Wei, M. M. Ackermans, E. M. Hutter, B. Ehrler, T. J. Savenije, *ACS Energy Lett.* **2020**, *5*, 3821.
[56] Y. Zhang, R. Wang, Y. Li, Z. Wang, S. Hu, X. Yan, Y. Zhai, C. Zhang, C. Sheng, *J. Phys. Chem. Lett.* **2019**, *10*, 13.
[57] A. Castellanos-Gomez, L. Vicarelli, E. Prada, J. O. Island, K. L. Narasimha-Acharya, S. I. Blanter, D. J. Groenendijk, M. Buscema, G. A. Steele, J. V. Alvarez, H. W. Zandbergen, J. J. Palacios, H. S. J. Van Der Zant, *2D Mater.* **2014**, *1*, 025001.
[58] D. Becker-Koch, B. Rivkin, F. Paulus, H. Xiang, Y. Dong, Z. Chen, A. A. Bakulin, Y. Vaynzof, *J. Phys.: Condens. Matter* **2019**, *31*, 124001.
[59] V. Mote, Y. Purushotham, B. Dole, *J Theor Appl Phys* **2012**, *6*, 6.
[60] J. Zipfel, M. Kulig, R. Perea-Causín, S. Brem, J. D. Ziegler, R. Rosati, T. Taniguchi, K. Watanabe, M. M. Glazov, E. Malic, A. Chernikov, *Phys. Rev. B* **2020**, *101*, 115430.
[61] Y. Dang, X. Liu, Y. Sun, J. Song, W. Hu, X. Tao, *J. Phys. Chem. Lett.* **2020**, *11*, 1689.
[62] M. Nespolo, A. H. Benahsene, *J. Appl. Crystallogr.* **2021**, *54*, 1594.
[63] K. Wagner, Z. A. Iakovlev, J. D. Ziegler, M. Cuccu, T. Taniguchi, K. Watanabe, M. M. Glazov, A. Chernikov, *Nano Lett.* **2023**, *23*, 4708.
[64] E. Wietek, M. Florian, J. Göser, T. Taniguchi, K. Watanabe, A. Högele, M. M. Glazov, A. Steinhoff, A. Chernikov, *Phys. Rev. Lett.* **2024**, *132*, 016202.
[65] D. Sun, Y. Rao, G. A. Reider, G. Chen, Y. You, L. Brézin, A. R. Harutyunyan, T. F. Heinz, *Nano Lett.* **2014**, *14*, 5625.